Soft Matter

PAPER

Wet granular rafts: aggregation in two dimensions under shear flow

Kai Huang,*[ab] Martin Brinkmann*[ac] and Stephan Herminghaus[a]

The aggregation and fragmentation of cohesive granular particles trapped at an air–liquid interface under shear flow are investigated by experiments and compared with numerical simulations. The cohesion owing to the formation of capillary bridges from a thin oil film covering the particles is found to dominate other particle–particle interactions. In the steady state the radius of gyration R_g of an N particle cluster follows a power law $R_g \propto N^{1/\delta}$. The fractal dimension δ of the clusters lies in the range between 1.5 and 1.6 and depends only weakly on the shear rate $\dot{\gamma}$. The probability to find a cluster of N particles or larger $P(N)$ displays an exponential tail $P(N) \propto \exp(-N/N_c)$ with a characteristic cluster size N_c. A power law $N_c \propto \dot{\gamma}^{-\beta}$ with an exponent $\beta = 0.65 \pm 0.06$ ($\beta = 0.68 \pm 0.02$) is found in our experiments (simulations). The fractal dimension of the clusters and the value of β are consistent with an estimate of the largest stable cluster based on the balance between the capillary force and the viscous drag force.

1 Introduction

Aggregation of macroscopic particles or bubbles trapped at an air–liquid interface into clusters is a common phenomenon that can be observed, *e.g.*, for cornflakes floating on milk, during a hot foam bath or in a glass of champagne.[1] The formation of these aggregates is driven by interfacial tension that is also responsible for the attraction and ordering of non-spherical objects such as tree needles or mosquito eggs floating at the water interface of a pond.[2] Applications based on the aggregation of particulate materials at interfaces are widespread and reach into industrial processes such as pharmaceutics, floatation processes in mining, and waste water treatment.[3–5] As a consequence, the structure, rheological behavior of the particle aggregates at interfaces, as well as their interactions with liquid interfaces within emulsions have attracted considerable interest over the past few decades.[6–10] Furthermore, a theory of interfacial particle aggregation and break-up can add to a better understanding of the rheology of Pickering emulsions.[11] From the perspective of fundamental research, the dynamics and self-organization of particles, emulsion droplets or bubbles at a fluid–liquid interface provide a well accessible model system to study, for example, colloidal crystals and glass transitions in two dimensions (2D).[12–18]

The spectrum of interactions between particles trapped in a fluid–liquid interface depends largely on the size of particles. For colloidal or submicron particles, the driving force behind aggregation is mainly due to van der Waals interaction and surface charges in the presence of electrolytes in the bulk liquid.[19–22] For particles with a diameter larger than tens of microns, *i.e.*, within the granular realm,[23,24] the typical interactions include monopolar forces such as the buoyancy force, dipolar forces due to the electrostatic charges at the interface, and the capillary forces mediated by deformations of the fluid–liquid interface.[1,25,26] For sub-millimeter particles focused here, the aggregation is mainly caused by the latter type of interaction.

The disintegration of dense particle clusters in the presence of shear flow has been extensively studied by Vassileva and co-workers.[27] They found that the critical shear rate required to break the aggregates depends weakly on their size, and is explained by a model considering the balance of the viscous drag and capillary interaction between particles. In a following work,[28] the breakup mechanisms, namely fragmentation and erosion, have been explored in detail.

In the present study, we focus on 2D *wet* granular clusters composed of sub-millimetric spherical glass beads trapped at an air–liquid interface. The beads are laden with a thin film of a secondary liquid immiscible with the viscous subphase. Upon contact this secondary liquid forms capillary bridges between adjacent particles, giving rise to a well-defined attractive particle–particle interaction.[29–32] This short ranged attractive force mediated by the capillary bridges is much stronger than the interactions which cause the clustering of 'dry' particles (without the secondary liquid). A quantitative comparison of the cluster size distributions in the steady state obtained from our experiment and our discrete elements method (DEM) simulations assuming frictionless soft core particles allows us to address the role of hydrodynamic interaction and interparticle friction. By considering the balance between the viscous drag force and the

[a]Max Planck Institute for Dynamics and Self-Organization, Am Fassberg 17, 37077 Göttingen, Germany. E-mail: martin.brinkmann@ds.mpg.de
[b]Experimentalphysik V, Universität Bayreuth, 95440 Bayreuth, Germany. E-mail: kai.huang@uni-bayreuth.de
[c]Experimental Physics, Saarland University, 66123 Saarbrücken, Germany

cohesive force of the capillary bridges we are able to relate the shear rate dependence of the cluster size distributions to the fractal dimension of the clusters.

This article is organized as follows: in the subsequent Section 2 we describe the experimental setup and the sample preparation procedure, the numerical methods used in the data analysis, and the physical model employed in the DEM simulations. In Section 3, the analyses of the structure and size distributions of the aggregates as well as a model based on the balance between the viscous drag force and the capillary force are presented.

2 Methods

2.1 Experimental setup and sample preparation

Spherical glass beads (Whitehouse scientific GP165) with diameters $D = (165 \pm 25)$ μm are cleaned subsequently with ethanol, acetone and purified water. After completely dried at $110°C$, the spheres were etched in an oxygen plasma (Harrick Plasma) and treated with a Piranha solution, *i.e.*, a $1:1$ volume mixture of concentrated sulfuric acid and hydrogen peroxide (35%). Subsequently, they are coated with OTS (octadecyltrichlorosilane) in a bicyclohexyl solvent (Fluka) and dried in a vacuum. After the treatment, the glass spheres are hydrophobic and exhibit a contact angle of $\approx 110°$ for an air–water interface as measured by optical microscopy.

The experimental setup to create the shear flow is illustrated in Fig. 1. The outer and inner cylinders of a Couette shear cell are driven independently by two stepper motors with angular velocities ω_o and ω_i, correspondingly. Pure glycerol with density $\rho_1 = 1.26$ g cm^{-3} and dynamic viscosity $\mu = 1.2$ Pa·s is filled in the cell up to a height of 10 cm. Assuming a linear velocity profile the shear rate is constant and can be determined by $\dot\gamma = |\omega_i r_i - \omega_o r_o|/\Delta r$, where $r_i = 4.5$ cm and $r_o = 6.5$ cm correspond to the radius of the inner and outer cylinder, respectively, and $\Delta r \equiv r_o - r_i$. This assumption is justified because the Reynolds number of the Couette flow, Re $= \rho_1 \dot\gamma \Delta r^2/\mu$, is smaller than 10 for the range of shear rates explored in our experiments.

As shown in Fig. 2(a), the hydrophobic glass spheres initially deposited onto the air–glycerol interface will pile up occasionally. A solution of silicone oil (AK5, Wacker) in hexane with a mass concentration of 0.1% is then applied to the air–glycerol interface. After completely immersing in the solution, the particles redistribute and form a monolayer, as indicated in Fig. 2(b). Driven by the evaporation front of the hexane, the packing of the spheres becomes more and more dense. As all the hexane evaporates, a monolayer of 'wet' granular clusters is obtained, *cf.* Fig. 2(c). Owing to the compact structure we refer to these clusters as 'wet' granular rafts. To quantify the amount of the added oil phase we employ the dimensionless concentration $W = V_o/V_p$, defined as the ratio of the volume V_o of the added oil to the total volume V_p of the particles. It is kept within a few percent so as to promote the formation of capillary bridges between adjacent particles instead of large liquid clusters, see also the image in Fig. 2(c).

The sketch in Fig. 1 illustrates how the aggregates floating on the air–liquid interface are illuminated from below by means of a collimated light source in combination with an annular mirror placed at the bottom of the Couette cell. Fig. 1(f) shows a top view of the 'wet' granular rafts in a steady state captured by the high speed camera (PCO h1200s). The captured image is in turn subjected to an image processing procedure, which is capable of detecting more than 95% of the particles in the field of view and locating the cluster boundaries, as illustrated in Fig. 1(g). To achieve a steady state, the sample is initially sheared at the largest possible shear rate 48.8 s^{-1} for 10 minutes, and with a desired shear rate for a period of 30 minutes.

2.2 Numerical simulations

The dynamics of the 'wet' particles in a linear shear flow is numerically simulated applying a two-dimensional discrete element model (DEM). To account for the polydispersity of the particle size in the experiments we consider a $1:1$ bidisperse mixture of spheres with radii $R_>$ and $R_<$, respectively, fixed by the ratio $\lambda \equiv R_>/R_< = 1.05$ of large to small radius and the mean particle diameter $D = R_< + R_>$. Each particle is assigned a mass $m_i = 4\pi\rho_p R_i^3/3$ where ρ_p is the mass density of the particles.

Particle–particle interactions are modeled employing a repulsive soft core potential and a constant attractive capillary force
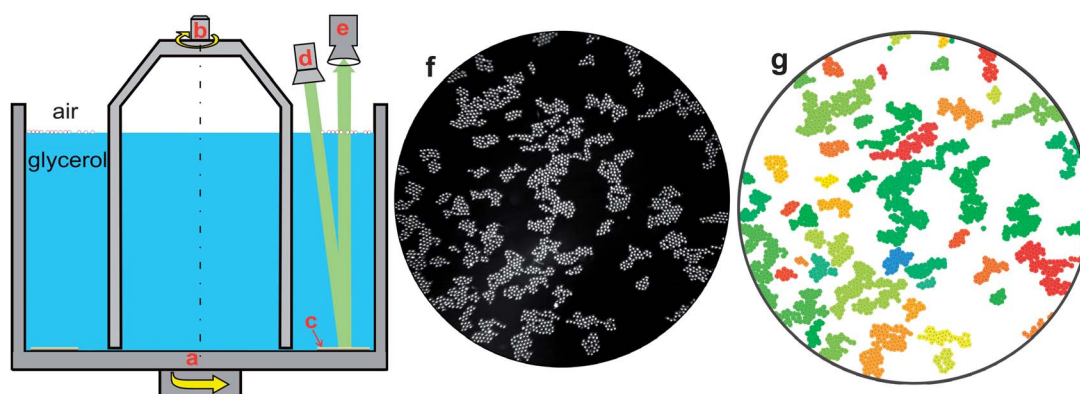
Fig. 1 Sketch of the experimental setup. The outer (a) and inner (b) cylinders of the Couette device are able to rotate independently at fixed angular velocities to create a linear shear profile in the gap. Hydrophobic glass spheres with a diameter of (165 ± 25) μm floating on glycerol are 'wet' by silicone oil. The particles are illuminated by parallel light emitted from the light source (d) and reflected by the mirror (c). Images of the aggregates are recorded in the top view (f) by a high speed camera (e) and subjected to an image processing procedure. Panel (g) shows a typical image after the image processing procedure. All particles in a cluster are displayed in the same color.
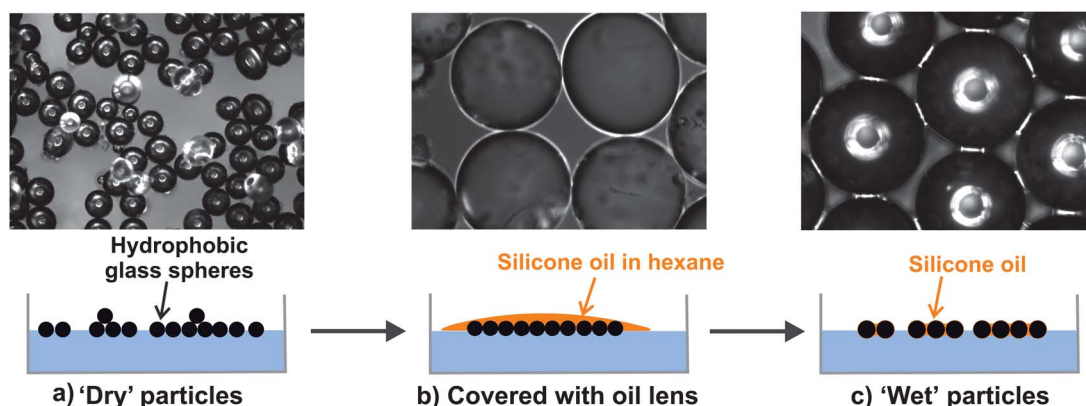
Fig. 2 Preparation of two-dimensional 'wet' granular clusters. The upper and lower rows show snapshots taken with an optical microscope and sketches to illustrate the procedure, respectively. (a) Initial state where particles are poured gently onto the air–glycerol interface; (b) particles covered by a lens composed of silicone oil solved in hexane; (c) particles bound together by capillary bridges (the white bars between adjacent particles) after evaporation of hexane.

acting below a finite separation. Tangential forces due to sliding or rolling friction, as well as dissipative normal forces are not considered, *i.e.*, two particles binding together *via* a liquid bridge can roll or slide freely relative to each other.

Following ref. 33 and 34 we chose an elastic repulsive interaction of the form

$$
\boldsymbol{f}_{ij}^{(r)} = \begin{cases} -\dfrac{3A}{2}\sqrt{|r_{ij} - R_i - R_j|}\,\boldsymbol{e}_{ij} & \text{for} \quad r_{ij} < R_i + R_j \\ 0 & \text{else} \end{cases} \tag{1}
$$

where r_{ij} is the distance from the center of particle i to the center of particle j with radii R_i and R_j, respectively, and $\boldsymbol{e}_{ij}$ is the unit vector pointing from the center of particle i to the center of particle j. The advantage of this non-linear spring force over, *e.g.*, a Hertzian contact is the diverging compressibility at zero indentation. The prefactor A in eqn (1) controls the particles' hardness.

To model the attractive capillary interaction we implemented the minimal capillary model proposed by Herminghaus in ref. 31 in our simulation code. At the same moment two particles touch, a capillary bridge is created which exerts an attractive force onto the particles. The capillary bridge is destroyed whenever the separation between the surfaces of the particles exceeds a certain threshold separation s^*.

The capillary force $\boldsymbol{f}_{ij}^{(c)}$ particle j exerts onto particle i is related to the interfacial tension of the wetting liquid and the radii of the particles by

$$
\boldsymbol{f}_{ij}^{(c)} = 2\pi\sigma\sqrt{R_i R_j}\,\boldsymbol{e}_{ij} \quad \text{for } r_{ij} < R_i + R_j + s^*, \tag{2}
$$

where $\boldsymbol{e}_{ij}$ is the unit vector pointing from the center of particle i to the center of particle j and σ is the interfacial tension of the air–liquid interface.

The spherical particles interact with the flow of the ambient liquid following Stokes' viscous drag force

$$
\boldsymbol{f}_i^{(d)} = 3\pi\mu R_i(\boldsymbol{v}_i - \dot{\gamma}x\boldsymbol{e}_y) \tag{3}
$$

for a sphere which is half immersed into the liquid. The dynamic viscosity of the ambient liquid is μ while $\dot{\gamma}$ denotes the shear rate.

The particle coordinate perpendicular to the direction of shear is denoted by x. We assume a linear flow profile which is not altered in the presence of the floating particles, *i.e.*, we do not account for any hydrodynamic interaction between the particles. To avoid boundary effects, and in consistency with the linear shear profile, we apply Lees Edward boundary conditions to the particles in the simulation box. For all simulation runs we set the side length of the square simulation box to $L = 80D$. To obtain the particle positions $\boldsymbol{r}_i(t)$ as a function of time t, Newton's equation of motion,

$$
m_i \ddot{\boldsymbol{r}}_i = \sum_{i \neq j}^{N_p} \boldsymbol{f}_{ij}^{(r)} + \sum_{j \in \mathscr{B}(i)} \boldsymbol{f}_{ij}^{(c)} + \boldsymbol{f}_i^{(d)}, \tag{4}
$$

is solved for every particle $i = 1, \ldots, N_p$ using a predictor corrector algorithm for second order ODEs. Here, the set $\mathscr{B}(i)$ is the set of particles $i \neq j$ which share a capillary bridge with particle i.

During each simulation run clusters of particles connected by capillary bridges are detected. Besides the cluster size distribution, we estimate distributions of the spatial extension of the clusters, and their elongation and orientation relative to the shear flow. For given coordinates $\boldsymbol{r}_i$ of the particles $i \in \mathscr{I}_\alpha$ in a cluster α, the latter quantities can be computed from the two-dimensional tensor

$$
\tilde{\boldsymbol{M}} = \frac{1}{N_\alpha} \sum_{i \in \mathscr{I}_\alpha} \boldsymbol{r}_i \otimes \boldsymbol{r}_i - \langle\boldsymbol{r}\rangle \otimes \langle\boldsymbol{r}\rangle \quad \text{with} \quad \langle\boldsymbol{r}\rangle = \frac{1}{N_\alpha} \sum_{i \in \mathscr{I}_\alpha} \boldsymbol{r}_i. \tag{5}
$$

Note that the definition of this tensor is similar to the moment of inertia tensor known in classical mechanics. Here, the index set $\mathscr{I}_\alpha$ contains all indices of particles being a part of cluster α, while the number of particles in the cluster is $N_\alpha = |\mathscr{I}_\alpha|$.

A number of quantities characterizing the geometry and orientation of a cluster can be deduced from $\tilde{\boldsymbol{M}}$. The radius of gyration R_g of the particle cluster is defined as

$$
R_g \equiv (\operatorname{tr} \tilde{\boldsymbol{M}})^{1/2}, \tag{6}
$$

while the ratio $\lambda = M_>/M_< > 1$ of the larger eigenvalue $M_>$ to the smaller eigenvalue $M_<$ of $\tilde{\boldsymbol{M}}$ can be employed to define the anisotropy of the cluster.

To non-dimensionalize all physical quantities relevant in our analysis we measure lengths and distances in units of the mean

diameter of the spheres, D, forces and energies in units of $F_0 \equiv \sigma D$ and $E_0 \equiv \sigma D^2$, respectively, and time in units of $T_0 \equiv \mu D/\sigma$. From $1/T_0$, one obtains the conversion factor between experimental and simulation shear rates to be 101 s^{-1}. Using this particular rescaling, we can set the mean particle diameter D, interfacial tension σ, and the dynamics viscosity μ to unity. Consequently, the mass and mass density of the particles is measured in units of $M_0 = \mu^2 D^2/\sigma$ and $\rho_p = \mu^2/\sigma D$, respectively.

Throughout all simulation runs we set the prefactor in the non-linear spring force eqn (1) to $A = 100\sigma D^{1/2}$. This guarantees to observe only small indentations between particles at small shear rates $\dot{\gamma} < T_0^{-1}$. Moreover, we set the rupture distance of the capillary bridges to $s^* = 0.1D$ independent of the radii of the particles. According to the analysis by Willett *et al.*[35] of the volume dependence of s^* on the liquid volume, this value corresponds to a liquid saturation of $W \approx 0.7\%$ as an upper limit, assuming six bridges on a bead. The integration time step is set to $\Delta T = 10^{-3} T_0$ in all simulation runs. Before starting the shearing motion of the liquid bath in our simulations, a number of $N = 1304$ particles where sequentially placed randomly in the box without overlaps resulting in a covered area fraction of 0.16. The total duration of a simulation run was set to $T_s = 200/\dot{\gamma}$, to ensure that the distribution of particle clusters is given enough time to relax into a stationary state. During the time interval $[0.5T_s, T_s]$, the size distribution of particle clusters connected by capillary bridges and their radius of gyration are sampled in regular intervals. Besides time averages over 20 measurements in each simulation run we take a further ensemble average over 20 realizations to improve the statistics.

3 Results and discussion

In this section, we first demonstrate the enhanced cohesion of 'wet' granular rafts by comparing the aggregates formed by the same particles without ('dry' case) and with ('wet' case) oil film for the same driving in subsection 3.1. For 'wet' aggregates, we then characterize their fractal dimensions and size distributions in subsections 3.2 and 3.3 correspondingly. Finally in subsection 3.4, we rationalize the scaling factors obtained in subsections 3.3 and 3.2 with a model based on the balance between the viscous drag force and the cohesive force.

3.1 'Dry' vs. 'wet' aggregates

Initially without shearing, we observe for both 'dry' and 'wet' particles an accumulation in the central region of the gap, along with the evaporation front of the volatile solvent hexane. As the steady state is reached after a certain time of shearing, the behavior of 'dry' and 'wet' aggregates are dramatically different, as shown in Fig. 3(a) and (b). For the case of 'dry' particles, no large scale heterogeneities are observed and the particles follow the shear flow. The dilation of 'dry' particles compared with the initial state is mainly due to the hard core repulsion between neighboring particles.

A different behavior is observed if a certain amount of oil is added to the solvent. In our experiments, we varied the volume fraction of oil in the range between $W \approx 0.5$ and 2.5%. In any case, large, persisting clusters are formed by the 'wet' particles. These clusters rotate around their center while following the
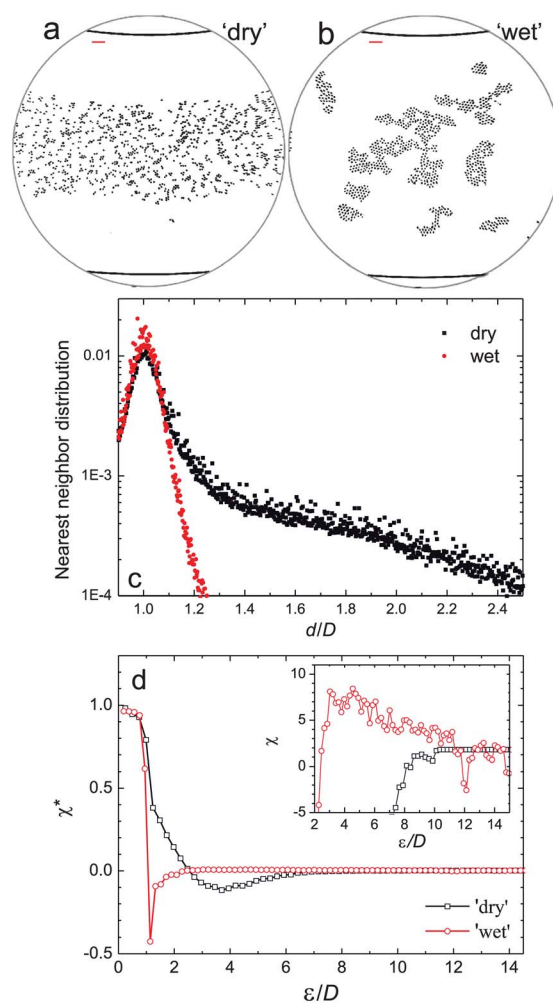
Fig. 3 Panels (a) and (b) display inverted sample images used for the morphological characterization for 'dry' and 'wet' particles, respectively, for a shear rate 7.3 s^{-1}, particle diameter $D = (165 \pm 25)$ μm, and a global area fraction of particles $\phi = 5.7\%$. Scale bar length 1 mm. (c) The nearest neighbor distribution for 'dry' and 'wet' particles as a function of the reduced distance d/D. (d) Euler characteristic χ^* for 'dry' and 'wet' particle aggregates normalized by the total number of particles as a function of the reduced disk diameter ε/D. Inset: a close view of the Euler characteristic χ (not normalized) around $\chi = 0$.

shear flow. During this motion they may also collide and merge, deform or break into several parts.

Inspection of the clusters by optical microscopy demonstrates that these clusters are formed by particles connected with each other through capillary oil bridges. The attractive forces induced by the bridges keep the particles in close contact. However, the relative positions of two merging clusters are not fixed at their first contact. Instead they could roll or slide with respect to each other until further contacts are formed that keep the newly formed structure stable. Generically, they are composed of a rigid backbone and floppy parts in their periphery. Folding or unfolding of clusters with chain-like structures under the shear flow could also be observed in some cases. As a result of the complex evolution, these 'wet' granular rafts are assemblies of dense, highly ordered domains which display a certain porosity on larger length scales.

Interactions between 'dry' particles can be explained by weak long-ranged capillary forces which are mediated by the distorted glycerol interface. These distortions are either caused by gravitational forces pushing the particles into the liquid interface or by the irregular shape of the three phase contact line which is pinned to the rough particle surface.[1,25] In the latter case, the capillary interaction depends on the relative orientation of the particles and may also be repulsive. Both interactions decay with a power law at medium separations on the scale of the particle diameter and are screened off by gravity on length scales larger than the capillary length of the glycerol–air interface. The above comparison indicates that the force owing to the formation of capillary bridges acting on adjacent particles dominates any other particle–particle interactions.

For a more quantitative characterization of the local arrangement of particles in 'wet' granular rafts we first computed the nearest neighbor distributions (NND) from our experimental data. To this end we detected the position of each particle with the image processing procedure proposed in ref. 36. This procedure is capable of locating more than 95% of the particles (on average ∼850 particles in each image) in the field of view. The statistics of the NND is further improved by averaging over 1000 frames.

As shown in Fig. 3(d), the decay of the distribution above a normalized distance $d/D = 1$, i.e., the mean particle diameter, is much faster for the 'wet' aggregates than for the 'dry' ones. There are almost no neighboring particles with $d/D > 1.3$, strongly suggesting that each 'wet' particle is connected to at least one neighbor via a capillary bridge. The broader distribution for assemblies of 'dry' particles clearly indicates that more particles are isolated as a result of the dilation driven by the shear flow. The mobility of the spheres arises from the viscous drag force which dominates the capillary interaction mediated by distortions of the liquid interface. Therefore no large clusters can be observed and the particles tend to follow the shear flow. However, it is difficult to quantify the formation of structures on length scales above the diameter of particles with the information of the NND alone.

To overcome this problem, we employ in addition the Euler characteristic of the particle distribution. The Euler characteristic, which is one of the three Minkowski measures in two dimensions, is particularly suited for this type of analysis because the Minkowski measures are well-known to capture all possible correlations within an ensemble of objects, by virtue of Hadwiger's theorem.[37] In this analysis, circular disks with diameter ε are placed at the center of each particle, and the set union of these disks is considered. The Euler characteristic χ of this set is defined as the number of disjoint objects minus the number of holes and is a function of the normalized disk diameter ε/D. Together with the other two Minkowski measures in two dimensions, the boundary length and the total area of the union set, it contains the same information on the particle configuration as all n-point correlation functions together.[37] We consider here only the Euler characteristic, as it contains the relevant information about the clustering of particles. As for the NND, we improve the statistics of the Euler characteristic by averaging over a large number of frames.

As shown in Fig. 3(e), the Euler characteristic χ for both 'dry' and 'wet' particles under shear flow shows a similar trend but is quantitatively very different. Here, we made use of the Euler characteristic $\chi^* \equiv \chi/N$ normalized by the particle number N for ε/D with $\chi \to 1$ as $\varepsilon/D \to 0$. While increasing the normalized disk diameter ε/D, the curves χ^* show a drop from 1 to a negative value followed by a slow increase. A drop of χ^* to a negative value indicates transition to a network-like structure. The sharp drop of χ^* for 'wet' aggregates shows that particle positions in 'wet' aggregates have a higher structural organization. The drop starts at $\varepsilon/D \approx 1$, because the merging of particles in contact reduces the number of objects and raises that of holes. Note that the slope drops much faster for the 'wet' case than for the 'dry' one, which is in accordance with the decay of NND for distances $d/D > 1$ discussed above. This sharp drop to negative values indicates that 'wet' particles have a much stronger tendency to form large and compact aggregates, since the number of holes increases substantially. The local minimum of χ^* gives rise to a characteristic value $\chi^*_{\min}$ and a corresponding characteristic disk size $\varepsilon_{\min}/D$, which are related to the local spatial structure of particles.

The parameter $\varepsilon_{\min}/D$ indicates a characteristic length above which the filling of holes starts to overwhelm the reduction of χ^* induced by the merging of clusters. We find $\varepsilon_{\min}/D \approx 1.14$ for the 'wet' particles, much smaller than the one for the 'dry' particles. This suggests that the holes in 'wet' aggregates are smaller than the ones in 'dry' aggregates. Moreover, the sudden jump of χ^* for the 'wet' case indicates that the closing of holes is much more coherent or, in other words, the holes have a much more uniform structure when compared to the 'dry' case.

The organization of the particles into extended clusters can be observed as a maximum of the Euler characteristic for large values $\varepsilon/D \gg 1$. The positive maximum of χ in the inset of Fig. 3 for 'wet' particles is a clear indication of dense aggregates while the corresponding curve for 'dry' particles does not display a maximum and approaches a constant value ≈ 1 from below. In this respect, it resembles qualitatively the form $\chi^* = (1 - \varepsilon/\ell)$ $\exp(-\varepsilon/\ell)$ derived for uncorrelated particle positions (Poisson process) with a length scale $\ell \equiv n^{-1/2}$, where n corresponds to the area density of particles.[38]

Besides the Euler characteristic, other statistical quantities such as pair correlation functions[26] and bond orientation order parameters[39,40] are also frequently used to characterize the local particle order in clusters. A further analysis of 'wet' granular rafts with these tools will be a focus of our further investigations.

The high prevalence of a locally hexagonal packing of particles in 'wet' granular clusters revealed from the above comparisons also enables us to identify clusters conveniently by reconstructing images with a disk size $\varepsilon/D > 2/\sqrt{3}$ (as shown in Fig. 1(g)). To account for the polydispersity in the radii of the glass beads, a disk radius $\varepsilon/D = \sqrt{3}$ is chosen for the analysis below. Based on this procedure, we can perform statistics on the properties of clusters including the fractal dimensions and cumulative size distributions, based on the snapshots from both experiments and DEM simulations.

3.2 Fractal dimension

A powerful approach to quantify the internal and overall structure of particle aggregates is to compute their fractal dimensions. This method has been successfully applied in a wide

range of problems, from the formation of galaxies to the growth of urban city.[41] Here we use the fractal dimension to characterize the structure of clusters formed under the shear flow in a steady state. In such a state, no temporal evolution of the cluster size distributions could be observed, although clusters keep deforming, breaking or merging with each other under the shear flow. To achieve good statistics, more than 4×10^4 clusters from recorded images taken under various steady states are analyzed. The fractal dimension δ is obtained from double logarithmic plots of the cluster size N and the average radius of gyration R_g of the clusters as defined by eqn (5) and (6).

Both experimental and simulation results, as shown in Fig. 4, suggest a quite well defined fractal dimension δ. The averaged value δ of the exponents from experiments (1.57 ± 0.03) and simulations (1.56 ± 0.03) agrees with each other, cf. the solid lines in Fig. 4. This agreement again indicates that the balance between the Stokes' drag force and the capillary force due to the formation of liquid bridges determines the dynamics of 'wet'

granular rafts, and it is appropriate to employ the minimal capillary model to describe the capillary force. Increasing the shear rate may lead to a slightly more fractal structure, as indicated by the subtle decrease of the fractal dimensions with increasing shear rate for the simulation results in a wider range of $\dot{\gamma}$, as shown in the inset of Fig. 4(b). This feature may be attributed to the reduced relaxation time for the clusters that are stretched under the shear flow. As the shear rate increases, the time for the floppy parts of the clusters to relax into a more stable structure via finding further possible bounds is limited, which presumably leads to a slightly more fractal structure.

The fractal dimension also offers a convenient classification of aggregates in two and three dimensions and has been used frequently to characterize aggregations of colloidal particles.[42] Typical fractal structures for colloidal aggregates are the diffusion-limited aggregation (DLCA) and the reaction-limited aggregation (RLCA), with characteristic fractal dimensions of 1.44 and 1.55 correspondingly for 2D systems.[19] In our system, the fractal dimension of sheared clusters consisting of 'wet' granular particles is closer to that of RLCA than DLCA. This is not surprising, because the mobility of the particles is governed by the shear flow instead of diffusion, and the binding of particles via the formation of capillary bridges is selective and reversible: only those capillary bridges strong enough to sustain the viscous drag force persist. In addition, the mixture of elongational flow and rotations leads to a permanent back-folding of more distant parts of the cluster onto its main body. This will clearly lead to a more compact structure of the granular rafts and a larger fractal dimension.

Further analysis of the scaling behavior reveals two features: first, there exists a slight change of the fractal dimension at a cluster size between 10 and 20, which presumably corresponds to the length scale of the rigid components of a cluster. While taking a closer look at the structure of clusters formed (see Fig. 3(b)), the branches of large clusters typically end with relatively more compact and rigid parts with a similar length scale. We anticipate that this type of rigid component is the basic unit to form a cluster. Further analysis based on an accurate definition and determination of those rigid components will be a focus of further investigations in order to decode further the physics behind this length scale. Second, the scattering of the rescaled gyration radius, R_g/D, also grows with the cluster size. This could be attributed not only to the statistical error, but also to the deformation of clusters under the shear flow as well as interactions between clusters. For example, multiple clusters may collide with each other and form transient clusters. They may break immediately or fold into more a compact cluster and survive for a longer time, which presumably depends on the balance between the number of bonds created and the total viscous drag force acting on various rigid parts of the cluster. Therefore, the larger the cluster size, the higher the probability is for a cluster to deform into various structures, i.e. various R_g.
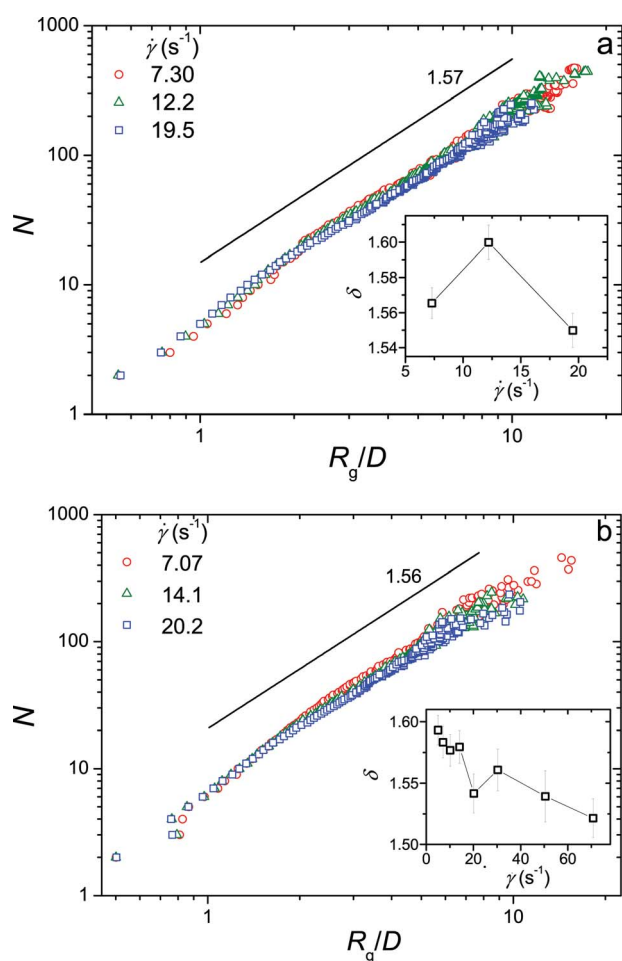
Fig. 4 The scaling between the number of particle in a cluster, N, and the gyration radius of the cluster rescaled by the averaged particle diameter, R_g/D, at various shear rates $\dot{\gamma}$ from both experiments (a) and DEM simulations (b). The liquid content for the experiments is $W = 1\%$. The solid line in both plots corresponds to the scaling averaged over all shear rates. See insets for the scaling δ at various shear rates. To have a better comparison, only three simulation results with shear rates closest to the experimental ones are shown in (b).

3.3 Cluster size distribution

For both experiments and DEM simulations, the cluster size distributions are obtained by counting the number of clusters with a certain size N (number of particles) for all the images captured. The distributions obtained in experiments are in a

steady state, because three distributions obtained with time intervals of 30 minutes agree with each other. Variations of the total simulation times show that 100 complete turns of the shear flow is already sufficient to reach a stationary distribution of cluster sizes. These distributions are also independent of the initial conditions: starting with $\dot{\gamma} = 0$ or $20\ \mathrm{s}^{-1}$ yields the same result, provided that the sample has been initialized with the desired shear rate. The global area fraction ϕ of the particles, defined as the area covered by the spheres over the total area of the interface, is also found to play a minor role, since a variation of ϕ from 10% to 25% does not lead to an apparent change of the size distribution. For the experimental results shown in Fig. 5(a), the global area fraction is around 10%, which is slightly higher at the center of the ring. In the DEM simulations, the area fraction is fixed to 16%.

Fig. 5(a) and (b) correspond to the cumulated cluster size distributions obtained from both experiments and DEM simulations. Here the cumulated probability $P(N)$ to find a cluster with N or more particles is preferred over a histogram because we mainly focus on the statistics at large N with typically low number of counts and because it facilitates comparisons owing to

the normalized initial value. In the experiment, counting starts from $N = 2$ to avoid the error counting of isolated particles at the image borders. For both experimental and simulation results, $P(N)$ decays exponentially with growing N for cluster sizes greater than ≈ 8, as the semi-log plot indicates. Different from the size distribution of droplets in an emulsion[43–45] and particle aggregates in three dimensional shear flow,[46] 'wet' granular rafts display a broader size distribution. Unlike a three dimensional liquid droplet that has the tendency to evolve into a spherical shape under the influence of interfacial tension, 'wet' granular rafts consist of densely packed rigid substructures, as the snapshots in Fig. 3 indicate. The existence of an internal structure dramatically enhances the number of possible breaking processes for larger clusters, and consequently contributes to the different size distributions. More detailed analysis of the size distribution in relation to the Smoluchowski rate equation[47,48] will be a focus of further investigation.

As the shear rate increases, the cluster size distribution decays faster, because the larger viscous drag force facilitates the breaking of clusters. To quantify the shear rate dependence of the distributions, we extract the decay constant k of the exponential
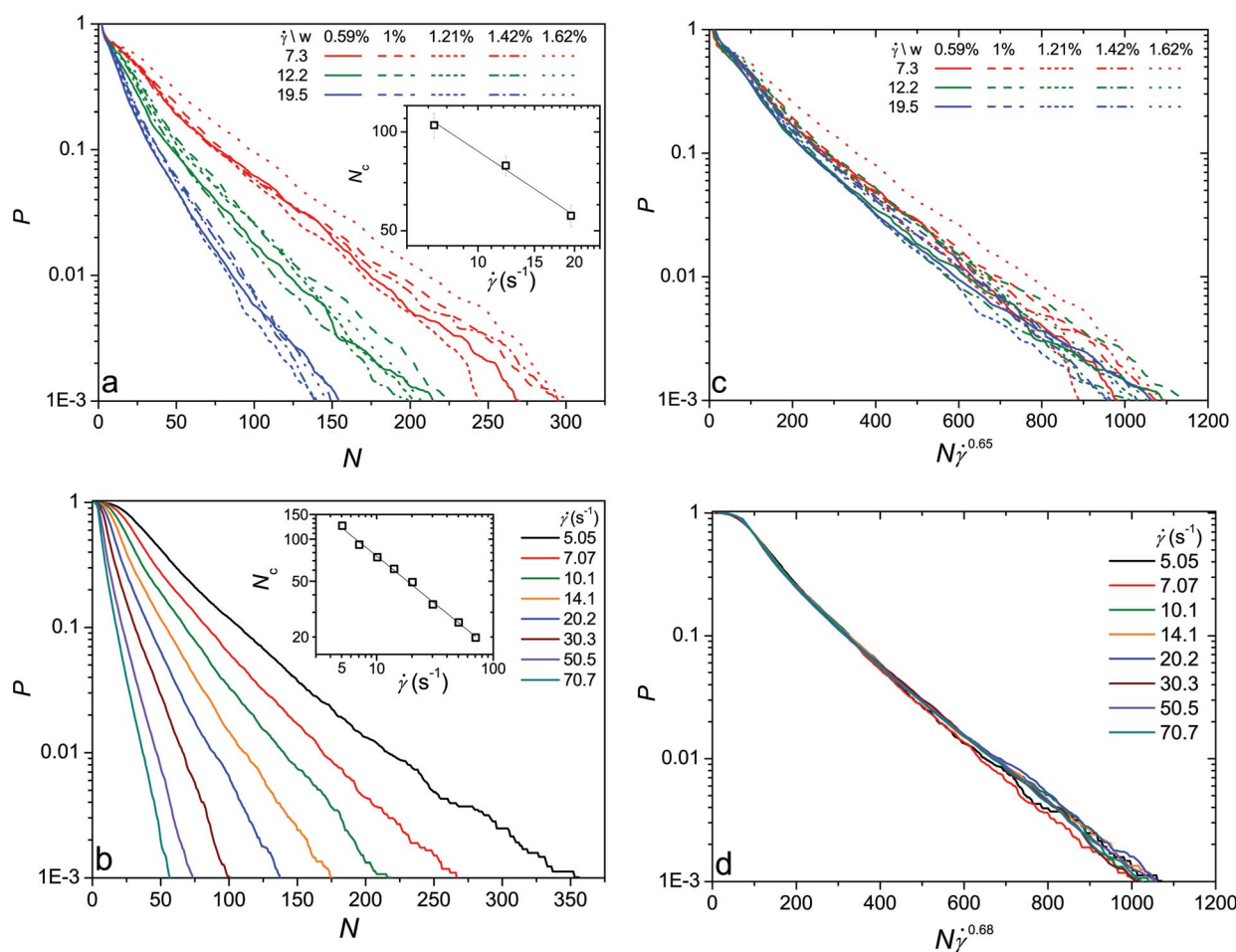
Fig. 5 Left: cumulative cluster size distribution P corresponding to the probability to find a cluster out of N or more particles. (a) Experimental results for various liquid contents W and shear rates $\dot{\gamma}$ and (b) corresponding results of DEM simulations. Insets show the scaling between the characteristic cluster size $N_c = k^{-1}$ and the shear rate $\dot{\gamma}$, where the decay rates k are obtained from linear fits of the corresponding data within the range $0.001 \leq P \leq 0.1$ in the semi-logarithmic plane. Right: corresponding P as a function of the rescaled cluster size $N\dot{\gamma}^{\beta}$. The exponent β for (c) experiment and (d) simulation corresponds to the scaling of N_c with $\dot{\gamma}$.

tails of the cumulative distributions $P(N)$ for various shear rates $\dot\gamma$. As shown in the insets of Fig. 5, the decay of the characteristic cluster size $N_c = k^{-1}$ with increasing shear rate $\dot\gamma$ follows a power law $N_c \propto \dot\gamma^{-\beta}$. The error bars in Fig. 5(a) correspond to the variation of the decay rate with the liquid content. The exponent $\beta = 0.65 \pm 0.06$ from our experimental data agrees with the corresponding value $\beta = 0.68 \pm 0.02$ derived from DEM simulations within the errorbar.

Different from the shear rate dependence in the experiments, varying the liquid content W will not influence the cluster size distribution dramatically as shown in Fig. 5(a). This suggests that the forces exerted onto adjacent particles by capillary bridges in our system barely depend on the bridge volume as described for pendular capillary water bridges in three-dimensional piles of spherical glass beads.[32] The higher probability for cluster sizes $N < 5$ in the experiment than that in the simulation could be attributed to the error counting of particles at the borders.

For the range of shear rates explored, the characteristic cluster size determined from the experiment is always larger than that from the simulation. This is presumably due to the reduced effective driving force arising from hydrodynamic screening. Other sources of this systematic difference may stem from the fact that the particles are not exactly half immersed into the viscous bath as assumed in our model. Another explanation for the systematic deviations may be linked to the tangential friction at the particle contacts: the additional work required to roll or slide two bounded particles could impede the formation and opening of cracks.

Utilizing the shear rate dependence obtained from the experiments, we are able to replot the cluster size distribution as a function of the rescaled cluster size $N\dot\gamma^{\beta}$. As shown in the right panels of Fig. 5, the collapse of the cumulative probabilities onto a master curve over the whole range of the rescaled cluster size $N\dot\gamma^{\beta}$ clearly demonstrates the power law dependence of the cluster size on the shear rate. A comparison between the data collapse obtained from the experiment in Fig. 5(c) and the simulation in Fig. 5(d) reveals a similar decay, which demonstrates the key role that the viscous drag force and the capillary force plays in determining the cluster size distributions.

Qualitatively, the shear rate dependence is plausible since the larger cluster experiences a larger viscous drag force which effectively increases the tensile stress in their center and tears them apart. In the following Section 3.4 we will introduce a model which is based on the balance between the viscous drag force and the capillary force. This model allows us to rationalize the power law scaling suggested by both the experiment and the simulation.

3.4 Model

The agreement between experiments and DEM simulations in the above analysis in terms of both the size distributions and structural aspects of the clusters suggests that the balance between the capillary force and the viscous drag force dominates the dynamics of 'wet' granular rafts. Following this idea, we developed a model based on the balance between the viscous drag force that deforms and eventually breaks the clusters and the attractive capillary forces that hold the particles in the cluster

together. Any linear shear profile, as the one used in our experiments, can be decomposed into two parts: a hyperbolic strain flow and a rotation (*cf.* Fig. 6(a)). As sketched in Fig. 6(b), the strain flow compresses the cluster in one direction and stretches it in an orthogonal direction. Thus the cluster, which continuously rotates in the frame of reference of the strain flow, will preferentially break along the direction of elongation, provided that the viscous drag force is large enough to overcome the capillary forces.

According to the Stokes' law, the viscous drag force acting on a single particle scales as $f^{(d)} \propto \mu D v$, where μ is the dynamic viscosity of the suspending liquid, D the diameter of the particle, and v the relative velocity of the particle in the hyperbolic flow field around the particle. For a cluster shown in Fig. 6(b), we assume that the stretching part of the viscous drag forces tends to break the cluster along the y axis, since it has different sign for the region with $x > 0$ (highlighted in Fig. 6(b) by the red transparent color) and that with $x < 0$. From the sketch Fig. 6(a), we see that the strain flow velocity in the x direction grows linearly with x: $v_x = \sqrt{2}\dot\gamma x/2$. Here, we use for convenience a coordinate system which is rotated by $45°$ with respect to the direction of the shear flow.

Thus we can calculate the total viscous drag force $F^{(d)}$ exerted on the cluster along the central cutting line $x = 0$ by integrating the drag force on a single particle $F^{(d)}$ over the red transparent region of the cluster. Assuming that the effective radius R_c of the region covered by the cluster is identical to the radius of gyration R_g, we have
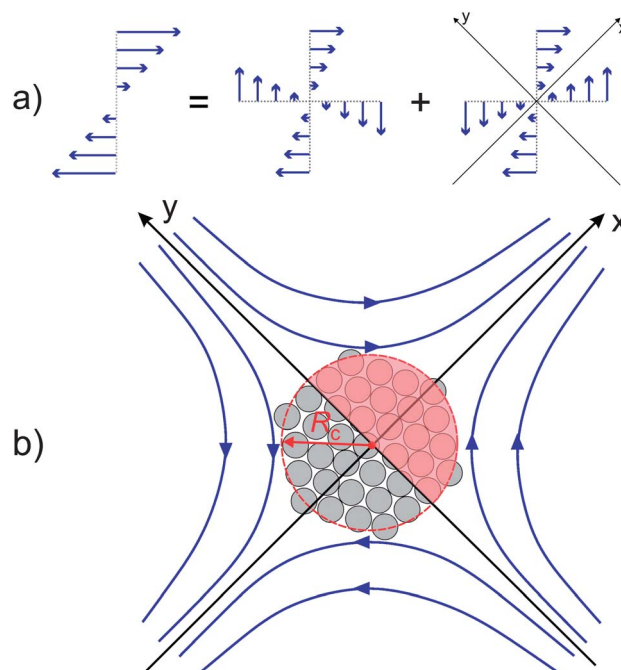
Fig. 6 (a) A sketch showing that any linear shear profile can be replaced by a superposition of a rotating and a hyperbolic straining flow field. (b) The hyperbolic stream lines of the hyperbolic flow profile will tend to compress the cluster with an effective radius R_c along the y axis and stretch it along the x axis. The center of the axes corresponds to the centroid of the cluster, and the half of the cluster located at $x > 0$ is highlighted by red color.

$$F^{(d)} = \int_{\mathcal{A}} f^{(d)} \phi \, dA \; \propto \; \mu \phi \dot{\gamma} R_g^3 / D, \qquad (7)$$

where $\phi \equiv ND^2/R_g^2 \propto N^{1-2/\delta}$ is the area fraction of particles in the cluster, and $\mathcal{A}$ is the area of a semi-circular region of the cluster with radius R_c, *cf.* also the sketch in Fig. 6.

On the other hand, the total capillary force $F^{(c)}$ acting along a cut $x = 0$ into the direction of the x axis can be estimated by[31]

$$F^{(c)} \propto n\sigma D \qquad (8)$$

where σ is the interfacial tension of the wetting liquid, n is the number of capillary bridges in a cut along the line $x = 0$.

To obtain the upper limit of the number of capillary bridges which have to be destroyed during a break-up, we assume that this number is proportional to the number of particles which are cut by the line $x = 0$. Then, the number of bridges per length in the cut is proportional to the area density ϕ, and we have $n \propto \phi R_g D$. This leads to the estimate

$$F^{(c)} \propto \sigma \phi R_g D^2 \qquad (9)$$

The maximum radius of gyration, R^*, of a stable particle cluster is reached when $F^{(c)} = F^{(d)}$, leading with eqn (7) and (9) to the estimate $R^* \propto \dot{\gamma}^{-1/2}$ and a maximum number of particles N^* following the scaling

$$N^* \propto \dot{\gamma}^{-\delta/2}. \qquad (10)$$

A lower limit for the size of the largest mechanically stable cluster can be derived from the assumption that the number of bonds that needs to be broken is independent of the size of the cluster. This picture may apply to a system where the particle clusters are build as a hierarchy of rigid subclusters. For example, two rigid subclusters are forming a rigid cluster after creation of only three new capillary bridges. Two of these rigid clusters can now merge to form a larger, rigid cluster and so on. In each hierarchy, we will have $F^{(c)} \propto \sigma D$ independent of ϕ and R_g leading to a scaling estimate of the form

$$N^* \propto \dot{\gamma}^{-\delta/(1+\delta)}. \qquad (11)$$

Both the experimental and simulation results showed that a scaling $N \propto R_g^{\delta}$ with $\delta \approx 1.6$ is valid over a wide range of N and only weakly dependent on the shear rate $\dot{\gamma}$. If we assume that the critical cluster size N^* scales linearly with the characteristic cluster size N_c we have $N_c \propto \dot{\gamma}^{-\beta}$ with an exponent in the range

$$\frac{\delta}{1+\delta} \leq \beta \leq \frac{\delta}{2}. \qquad (12)$$

By explicit calculation, we indeed find that the values of β are consistent with the scaling estimates for both our experimental data and our simulation data: assuming $\delta \approx 1.6$, we obtain a lower bound $\beta_{min} \approx 0.6$ and an upper bound $\beta_{max} \approx 0.8$ for β. It is remarkable that the values of both experiments and the DEM simulations lie closer to the lower bound that corresponds to the assumption of a constant number of contacts that need to be destroyed in a cluster break-up. This agrees with the qualitative analysis based on visual inspections described in Section 3.1.

Besides the viscous drag force, inertial forces arising from the rotation of the clusters may also play a role in the break up of clusters. The internal force acting on a single particle scales as $f^{(i)} \propto \rho_p D^3 \dot{\gamma}^2 r$, with r being the distance to the cluster center. The power of the spatial dependence of the relevant component on the inertial force and that of the viscous drag force on the elongational flow is identical. Similar to the viscous forces the inertial forces acting in the x-direction on the upper half of the cluster act on the cut along the y-axis. It is immediately clear that the viscous force is dominant for small shear rates and that the inertial forces becomes prominent for shear rates $\dot{\gamma} \gtrsim \mu/\rho_p D^2 \approx 105 \text{ s}^{-1}$, only. Inertial effects can be safely neglected as the shear rate used in our experiments is much smaller.

Similar criteria have also been used to describe the breaking of aggregates trapped at an air–water interface under shear flow.[27] The attraction between particles in that case is due to the force arising from gravity-induced interfacial deformations[25] that corresponds to the 'dry' situation in our current investigation. Despite this difference, the criteria based on the force balance could explain the size of aggregates for both cases.

4 Conclusion and outlook

It has been shown that cohesive spherical particles trapped at an air–liquid interface aggregate into clusters with a characteristic size in the presence of a linear shear flow. In our experiments, the cohesive particles are prepared by introducing an immiscible second liquid that adheres to the surface of submillimetric glass beads. Capillary bridges formed by the oil phase on the surface induce a strong attractive force which dominates all other particle–particle interactions and leads to the formation of 'wet' granular rafts. In corresponding DEM simulations of particle aggregation in shear flow, the capillary force is modeled by a short ranged attractive force between adjacent particles.

The cohesion induced by the second liquid is demonstrated to dominate other particle–particle interactions, as a comparison of the snapshots to the 'dry' case reveals. The Euler characteristic shows that this strong cohesion leads to a closer packing of the particles into extended clusters. We were able to show that the size of the clusters and their gyration radius follow a power law scaling over at least one and a half order of magnitudes. Their fractal dimension δ, as revealed by both experiments and simulations, is in a range between 1.5 and 1.6, with a weak dependence on the shear rate. The values are closer to those of RLCA in 2D than for 2D DLCA. The cumulated size distribution in the steady state decays exponentially with the number of particles in the clusters. The characteristic cluster size N_c decreases with increasing shear rate. In addition, we could demonstrate that the experimentally measured cluster size distributions depend only weakly on the amount of wetting liquid in accordance with the known fact that the force between spherical bodies induced by an axially symmetric pendular bridge approaches a constant value in the limit of small volumes.

The scaling of the characteristic cluster size $N_c \propto \dot{\gamma}^{-\beta}$ with the shear rate is consistent with a model considering the balance between the viscous drag force that tends to break the cluster and the capillary force that binds particles together. This balance, together with the fractal dimension δ, provides an estimated scaling relationship between the cluster size and shear rate which agrees fairly well with the values of the exponent $\beta = 0.65 \pm 0.06$

obtained from experiments and 0.68 ± 0.02 derived from DEM simulations.

The strong cohesion forces arising from the capillary bridges and their robustness against changes in the thickness of the oil film covering the particles qualify this system as a suitable model system to study the dynamics of driven wet granular matter in two dimensions. For the particle size chosen gravity does not play an important role, and the particles are driven homogeneously by the linear shear profile. Besides the importance as a model system, this investigation also suggests to enhance the efficiency of particle aggregation by wetting films. This may be relevant for a number of applications, such as waste water treatments and ore handling.

Further characterizations of the aggregation will be focused on the anisotropy, the dynamics of the rigid components of a cluster, and the scaling with other control parameters such as viscosity and surface tension. By simulation, we would also like to check the role that hydrodynamic interactions play in such a system. At a sufficient large area fraction, the 'wet' particles under shear flow may self-organize themselves into a single large cluster. The dynamical behavior of such a cluster could help to elucidate fundamental questions about melting or jamming transitions[49,50] of cohesive and non-cohesive materials in two dimensions. In addition, it could also shed light on the stability mechanism of bicontinuous interfacially jammed emulsion gels.[7,9]

Acknowledgements

References

1 D. Stamou, C. Duschl and D. Johannsmann, *Phys. Rev. E: Stat. Phys., Plasmas, Fluids, Relat. Interdiscip. Top.*, 2000, **62**, 5263–5272.
2 J. C. Loudet and B. Pouligny, *Eur. Phys. J. E: Soft Matter Biol. Phys.*, 2011, **34**, 76.
3 *Colloidal Dispersions*, ed. W. B. Russel, D. A. Saville and W. R. Schowalter, Cambridge University Press, Cambridge, England, 1989.
4 G. M. Whitesides and B. Grzybowski, *Science*, 2002, **295**, 2418–2421.
5 B. A. Wills, *Mineral Processing Technology*, Butterworth-Heinemann, Oxford, UK, 6th edn, 1997.
6 H. A. Stone, *Annu. Rev. Fluid Mech.*, 1994, **26**, 65–102.
7 K. Stratford, R. Adhikari, I. Pagonabarraga, J. C. Desplat and M. E. Cates, *Science*, 2005, **309**, 2198–2201.
8 B. P. Binks and T. S. Horozov, *Colloidal Particles at Liquid Interfaces*, Cambridge University Press, 2006.
9 M. E. Cates and P. S. Clegg, *Soft Matter*, 2008, **4**, 2132.
10 G. G. Fuller and J. Vermant, *Annu. Rev. Chem. Biomol. Eng.*, 2012, **3**, 519–543.
11 E. Koos and N. Willenbacher, *Science*, 2011, **331**, 897–900.
12 P. Pieranski, *Phys. Rev. Lett.*, 1980, **45**, 569.
13 K. Zahn, R. Lenke and G. Maret, *Phys. Rev. Lett.*, 1999, **82**, 2721–2724.
14 K. Zahn and G. Maret, *Phys. Rev. Lett.*, 2000, **85**, 3656–3659.
15 M. G. Nikolaides, A. R. Bausch, M. F. Hsu, A. D. Dinsmore, M. P. Brenner, C. Gay and D. A. Weitz, *Nature*, 2002, **420**, 299.
16 P. Cicuta, E. J. Stancik and G. G. Fuller, *Phys. Rev. Lett.*, 2003, **90**, 236101.
17 C. Eisenmann, U. Gasser, P. Keim and G. Maret, *Phys. Rev. Lett.*, 2004, **93**, 105702.
18 J. J. Cerdà, T. Sintes, C. Holm, C. M. Sorensen and A. Chakrabarti, *Phys. Rev. E: Stat., Nonlinear, Soft Matter Phys.*, 2008, **78**, 031403.
19 D. J. Robinson and J. C. Earnshaw, *Phys. Rev. A*, 1992, **46**, 2045–2054.
20 P. Pieranski, *Phys. Rev. Lett.*, 1980, **45**, 569–572.
21 P. J. Lu, J. C. Conrad, H. M. Wyss, A. B. Schofield and D. A. Weitz, *Phys. Rev. Lett.*, 2006, **96**, 028306.
22 V. N. Manoharan, M. T. Elsesser and D. J. Pine, *Science*, 2003, **301**, 483.
23 *Powders and Grains*, ed. R. Garcia-Rojo, H. J. Herrmann and S. McNamara, Taylor & Francis, London, 2005.
24 J. Duran, *Sands, Powders and Grains: An Introduction to the Physics of Granular Materials*, Springer-Verlag, New York, Inc., 1st edn, 2000.
25 N. D. Vassileva, D. van den Ende, F. Mugele and J. Mellema, *Langmuir*, 2005, **21**, 11190–11200.
26 H. Hoekstra, J. Vermant, J. Mewis and G. G. Fuller, *Langmuir*, 2003, **19**, 9134.
27 N. D. Vassileva, D. van den Ende, F. Mugele and J. Mellema, *Langmuir*, 2006, **22**, 4959–4967.
28 N. D. Vassileva, D. van den Ende, F. Mugele and J. Mellema, *Langmuir*, 2007, **23**, 2352–2361.
29 C. Camoin and R. Blanc, *J. Phys., Lett.*, 1985, **46**, 67–74.
30 W. A. Goedel, *Europhys. Lett.*, 2003, **62**, 607.
31 S. Herminghaus, *Adv. Phys.*, 2005, **54**, 221–261.
32 M. Scheel, R. Seemann, M. Brinkmann, M. Di Michiel, A. Sheppard, B. Breidenbach and S. Herminghaus, *Nat. Mater.*, 2008, **7**, 189–193.
33 C. S. O'Hern, L. E. Silbert, A. J. Liu and S. R. Nagel, *Phys. Rev. E: Stat., Nonlinear, Soft Matter Phys.*, 2003, **68**, 011306.
34 S. H. E. Rahbari, J. Vollmer, S. Herminghaus and M. Brinkmann, *Phys. Rev. E: Stat., Nonlinear, Soft Matter Phys.*, 2010, **82**, 061305.
35 C. Willett, *Langmuir*, 2000, **16**, 9396–9405.
36 J. C. Crocker and D. G. Grier, *J. Colloid Interface Sci.*, 1996, **179**, 298–310.
37 K. R. Mecke, T. Buchert and H. Wagner, *Astron. Astrophys.*, 1994, **288**, 697–704.
38 K. R. Mecke and D. Stoyan, *Biom. J.*, 2005, **47**, 473–488.
39 P. J. Steinhardt, D. R. Nelson and M. Ronchetti, *Phys. Rev. B: Condens. Matter Mater. Phys.*, 1983, **28**, 784–805.
40 W. Lechner and C. Dellago, *J. Chem. Phys.*, 2008, **129**, 114707.
41 P. Meakin, *Fractals, Scaling and Growth Far from Equilibrium*, Cambridge University Press, 1998.
42 M. Lin, H. M. Lindsay, D. A. Weitz, R. C. Ball, R. Klein and P. Meakin, *Nature*, 1989, **339**, 360.
43 D. Ramkrishna, *Population Balances: Theory and Applications to Particulate Systems in Engineering*, Academic Press, San Diego, 2000.
44 P. Becher, *Emulsions: Theory and Practice*, American Chemical Society, Oxford University Press, Washington, D.C., Oxford, 2001.
45 N. B. Raikar, S. R. Bhatia, M. F. Malone, D. J. McClements and M. A. Henson, *Ind. Eng. Chem. Res.*, 2011, **50**, 6089–6100.
46 A. Tolpekin, M. H. G. Duits, D. van den Ende and J. Mellema, *Langmuir*, 2003, **20**, 2614–2627.
47 F. Family, P. Meakin and J. M. Deutch, *Phys. Rev. Lett.*, 1986, **57**, 727–730.
48 S. Kumar and D. Ramkrishna, *Chem. Eng. Sci.*, 1996, **51**, 1311–1332.
49 A. J. Liu and S. R. Nagel, *Soft Matter*, 2010, **6**, 2869.
50 D. Bi, J. Zhang, B. Chakraborty and R. P. Behringer, *Nature*, 2011, **480**, 355–358.